Passivity-Based Stability Analysis and Generic Controller Design for Grid-Forming Inverter

Guotao Wu, *Student Member, IEEE*, Yuying He, *Member, IEEE*, Hao Zhang, *Student Member, IEEE*, Xuehua Wang, *Member, IEEE*, Donghua Pan, *Member, IEEE*, Xinbo Ruan, *Fellow, IEEE*, and Chuan Yao

***Abstract*—With the remarkable growth of renewable energy resources, the grid-forming (GFM) inverter with the function of grid voltage/frequency support attracts much attention. Due to the inverter-grid interaction, the stability of the GFM inverter is a critical issue. The passivity-based analysis approach, which was widely applied to the conventional grid-following inverter, has been proved to be promising. Yet, its application to the GFM inverter is still insufficient. To this end, this article conducts a comprehensive passivity-based analysis for the GFM inverter with single-loop voltage control. It finds that the two indices of the passivity-based stability criterion, i.e., the individual stability and the output impedance passivity, bring identical constraints on the voltage controller, and the passivity cannot be ensured with typical voltage controllers. To shrink the unexpected nonpassive frequency ranges, a generic grid-current feedforward scheme is explored, and the proper feedforward functions compatible with different voltage controllers are derived. With the proposed scheme, the passivity can be guaranteed up to the Nyquist frequency. Finally, experimental results from a 6-kVA prototype are provided to verify the theoretical analysis.**

***Index Terms*—Feedforward, grid-forming (GFM) inverters, passivity, single-loop voltage control.**

I. Introduction

With the remarkable growth of renewable energy resources, the distributed power generation systems, which are generally connected to the power grid via voltage source inverters (VSIs), are starting to take over the dominant role from synchronous machines (SMs) [1], [2], [3], [4]. The VSIs can be classified into two types, namely grid-following (GFL) and grid-forming (GFM) inverters. The former works essentially as a current source, which controls the ac-side current and follows the phase angle of the grid voltage via the phase-locked loop [5]. In contrast, the latter behaves as a voltage source and participates in forming the system voltage [6], [7]. In recent decades, attentions are gradually turned into the GFM inverter, owing to its SM-like characteristics and capability of operating in weak grid condition or even forming a stand-alone grid.

Due to the inverter-grid interaction, the stability of the GFM inverter is a critical issue [8]. The eigenvalue-based analysis approach is usually used for stability prediction, which models the system with the integration of grid impedance and predicts the stability from its eigenvalues [9]. However, it is difficult to model the system under a complex grid impedance condition. Alternatively, the impedance-based approach is attractive which predicts the stability from the ratio of the inverter output impedance to the grid impedance [10]. This approach is further extended to the complicated inverter-based multibus ac power systems in [11] and [12], where the component connection method and sequence impedance-based method are propelled to release the computation burden. It should be noticed that the impedance-based approach requires repeatedly to assess the stability when the grid impedance varies. Given that the grid impedance is uncertain and varies in a wide range in practice, the passivity-based approach is more promising [13], [14]. It tells that the system stable operation requires: 1) the inverter is individually stable and 2) its output impedance is passive, which reflects the terminal behavior of the VSI—dissipating energy. For convenience, they are called as "individual stability" and "output impedance passivity" hereinafter, respectively.

The passivity-based analysis method has been extensively applied to the GFL inverter [15], [16], [17], [18]. However, the studies on the passivity of the GFM inverter are still insufficient [19], [20], [21]. Until recently, it was revealed that its passivity in high-frequency range (e.g., from 200 Hz up to the Nyquist frequency), which is dominated by the voltage control, can hardly be ensured due to the impact of digital control delay [19]. The voltage control schemes can be classified into two categories, i.e., the single-loop control and the dual-loop control, with respect to the number of feedback control variables. The former directly regulates the output voltage across the *LC* filter

Manuscript received 11 November 2022; accepted 6 January 2023. Date of publication 18 January 2023; date of current version 10 March 2023. This work was supported by the National Natural Science Foundation of China under Grant 52277181. Recommended for publication by Associate Editor H. L. Ginn. *(Corresponding author: Yuying He.)*

Guotao Wu, Hao Zhang, and Xuehua Wang are with the State Key Laboratory of Advanced Electromagnetic Engineering and Technology, School of Electrical and Electronic Engineering, Huazhong University of Science and Technology, Wuhan 430074, China (e-mail: wuguotaozero@nwsuaf.edu.cn; zhangh98@hust.edu.cn; wang.xh@hust.edu.cn).

Yuying He is with the College of Energy and Electrical Engineering, Hohai University, Nanjing 211100, China (e-mail: heyuying@hhu.edu.cn).

Donghua Pan is with the State Key Laboratory of Advanced Electromagnetic Engineering and Technology, School of Electrical and Electronic Engineering, Huazhong University of Science and Technology, Wuhan 430074, China, and also with the GoodWe Technologies Co., Ltd., Suzhou 215011, China (e-mail: pan.dh@outlook.com).

Xinbo Ruan is with the State Key Laboratory of Advanced Electromagnetic Engineering and Technology, School of Electrical and Electronic Engineering, Huazhong University of Science and Technology, Wuhan 430074, China, and also with the Center for More-Electric-Aircraft Power Systems, College of Automation Engineering, Nanjing University of Aeronautics and Astronautics, Nanjing 210016, China (e-mail: ruanxb@nuaa.edu.cn).

Chuan Yao is with the Wuhan Second Ship Design and Research Institute, Wuhan 430064, China (e-mail: yaochuan_hbwh@163.com).

Color versions of one or more figures in this article are available at https://doi.org/10.1109/TPEL.2023.3237608.

Digital Object Identifier 10.1109/TPEL.2023.3237608

capacitor, while the latter adds an inner inductor-current loop to emulate a virtual resistor and thereby dampen the *LC* filter resonance. Due to the digital control delay, this virtual resistor becomes negative in the frequency range above one-sixth of the sampling frequency, jeopardizing the passivity property of the GFM inverter [22]. In [19], an extra inductor-current feedback active damping combined with the grid-current feedforward is introduced, which widens the passive range at the cost of complex algorithm. In contrast, the passivity enhancement for the single-loop control is easier. It is revealed in [20] that the passivity can be secured with only the proportional grid-current feedforward scheme co-designed with the pure resonant (R) voltage controller. Cao et al. [21] proposed the adaptive current feedforward approach, which achieves the passivity at the resonance frequency. Yet, those works only consider a specific single-loop voltage controller. The passivity properties of other commonly-used voltage controllers, such as proportional resonant (PR) controller [23] and resonant-phase lag filter (R-PLF) controller [24], are still unclear. Moreover, the relation between the individually stable range and the passive range of output impedance has far yet been discussed. These will be answered in this article.

Focusing on the GFM inverter with single-loop voltage control, this article conducts a comprehensive passivity-based analysis and proposes a generic controller design method. The contributions of this article are summarized as follows.

1) The finding is drawn that, the individually stable range of the GFM inverter with single-loop voltage control is identical with the passive range of output impedance.
2) The graphical passivity-based evaluation is conducted for the GFM inverter with PR, R, and R-PLF voltage controllers. It reveals that the phase lag of voltage controller actually contributes to the system passivation.
3) The grid-current feedforward scheme is explored from the view of impedance reshaping. Feedforward functions matched to different voltage controllers are summarized, which extend the passive range up to the Nyquist frequency.

The rest of this article is organized as follows. In Section II, the impedance model of the GFM inverter with single-loop voltage control is derived. In Section III, based on this model, the relation between the individually stable range and the passive range of output impedance is revealed, and then the passive performances of typical voltage controllers are thoroughly evaluated. In Section IV, the passivity enhancement via grid-current feedforward is explored. Experimental results for validation are presented in Section V. Finally, Section VI concludes this article.

II. System Description and Modelling

A. System Description

Fig. 1 shows the configuration of a three-phase GFM inverter, where $V_{\rm dc}$ and v_{inv} represent the input dc-link voltage and the midpoint voltage of bridge arm, respectively. The inductor L and the capacitor C form an output filter. Z_g represents the grid impedance at the point of common coupling (PCC).

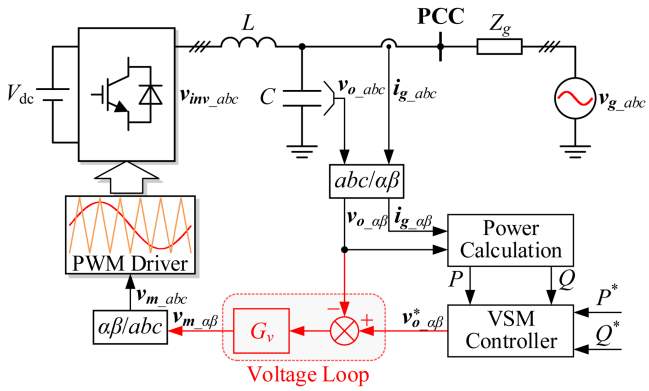

Fig. 1. Configuration of a three-phase GFM inverter with single-loop voltage control.

To maintain the grid voltage and frequency, the closed-loop control consisting of an outer power loop and an inner voltage loop is required. As shown in Fig. 1, the output active power P and reactive power Q, calculated by the instantaneous power theory [25], are fed into the virtual synchronous machine (VSM) power controller to generate the voltage reference v_o^* [26]. The voltage controller G_v in the $\alpha\beta$ frame is employed to ensure that the capacitor voltage v_o tracks the reference v_o^* accurately. After applying the $\alpha\beta$/*abc* transformation, the output of the voltage controller is then processed by the pulsewidth modulation (PWM), generating the control signals of power switches.

B. Output Impedance Modeling

In general, the dynamics of the outer power loop is over ten times slower than that of the inner voltage loop [27]. Since we focus on the stability issue determined by the voltage loop, the power loop is neglected in the modeling process, and the conclusion remains valid even with considering the impact of the power loop control. Furthermore, since the transfer function of the plant and the voltage controller are symmetrical in the $\alpha\beta$ frame, the system can be represented by a single-input and single-output (SISO) model, as shown in Fig. 2(a). Therein, $G_d(s)$ denotes the computation and PWM delays, expressed as

$$G_d(s) \approx e^{-1.5sT_s} \tag{1}$$

where T_s is the sampling period.

Via series of equivalent transformations, Fig. 2(a) can be normalized to a dual-input-single-output form, as shown in Fig. 2(b), where

$$G_{x1}(s) = \frac{G_v(s)\,G_d(s)}{Ls} \tag{2}$$

$$G_{x2}(s) = \frac{Ls}{LCs^2+1}. \tag{3}$$

From Fig. 2(b), the loop gain $T(s)$ can be derived as

$$T(s) = G_{x1}(s)\,G_{x2}(s) = G_v(s)\,G_d(s)\,\frac{\omega_r^2}{s^2+\omega_r^2} \tag{4}$$

with ω_r being the *LC* resonant angular frequency

$$\omega_r = 2\pi f_r = 1/\sqrt{LC}. \tag{5}$$

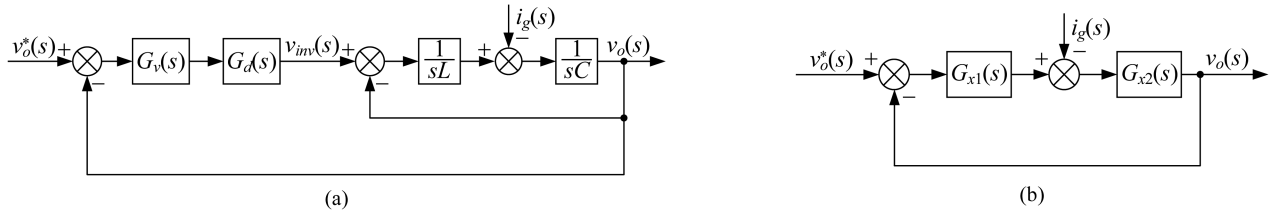

Fig. 2. SISO control block diagram of the digitally controlled GFM inverter with single-loop voltage control. (a) Initial form. (b) Equivalent form.

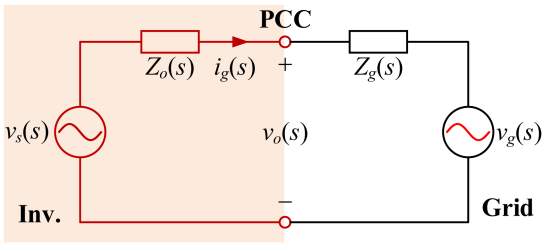

Fig. 3. Equivalent circuit of the grid-connected system.

Meanwhile, the output voltage v_o can be derived as

$$v_o(s) = v_s(s) - Z_o(s)\, i_g(s) \tag{6}$$

where

$$v_s(s) = \frac{T(s)}{1+T(s)} v_o^*(s) \tag{7}$$

$$Z_o(s) = \frac{G_{x2}(s)}{1+T(s)}. \tag{8}$$

III. Passivity-Based Stability Analysis

A. Passivity-Based Stability Criterion

According to (6), the GFM inverter can be modeled by its Thevenin equivalent circuit, consisting of an ideal voltage source $v_s(s)$ in series with the output impedance $Z_o(s)$, as shown in Fig. 3. Besides, the grid is modeled by the ideal voltage source $v_g(s)$ in series with the grid impedance $Z_g(s)$. Accordingly, the output voltage $v_o(s)$ can also be written as

$$\begin{aligned} v_o(s) &= \frac{Z_g(s)}{Z_o(s)+Z_g(s)} v_s(s) + \frac{Z_o(s)}{Z_o(s)+Z_g(s)} v_g(s) \\ &= \underbrace{\left[v_s(s) + \frac{Z_o(s)}{Z_g(s)} v_g(s)\right]}_{\text{First item}} \cdot \underbrace{\frac{1}{1+Z_o(s)/Z_g(s)}}_{\text{Second item}}. \end{aligned} \tag{9}$$

As shown in (9), the output voltage $v_o(s)$ can be constituted by two items. Obviously, $v_o(s)$ will be stable if these two parts are both stabilized.

Since the number of poles of $v_s(s)$ and $Z_o(s)$ are same, the first item is stable if $v_s(s)$ has no right-half-plane (RHP) poles. This implies the GFM inverter should be individually stable.

The second item is related to the interaction between the GFM inverter and the power grid. It can be regarded as an equivalent closed-loop system, where the forward gain is unity and the feedback gain is $Z_o(s)/Z_g(s)$. Accordingly, the stability can be examined by the phase margin (denoted by $\mathrm{PM}_{\mathrm{int}}$), i.e.,

$$\mathrm{PM}_{\mathrm{int}} = \pi - \left[\angle Z_o\left(j\omega_{\mathrm{int}}\right) - \angle Z_g\left(j\omega_{\mathrm{int}}\right)\right] \tag{10}$$

where $\omega_{\mathrm{int}} = 2\pi f_{\mathrm{int}}$ is the intersection angular frequency of $Z_o(s)$ and $Z_g(s)$ in the magnitude plots.

According to the Nyquist stability criterion, the sufficient and necessary stability condition is $\mathrm{PM}_{\mathrm{int}} > 0$. Generally, $\angle Z_g(s)$ is within $[-\pi/2, \pi/2]$. Thus, in order to ensure $\mathrm{PM}_{\mathrm{int}} > 0$, it is preferable to bound $\angle Z_o(s)$ within $[-\pi/2, \pi/2]$ in the entire frequency range. Therefore, a sufficient but not necessary stability condition for the grid-connection system, termed as passivity, is described as follows.

1) GFM inverter must be individually stable.
2) Phase of output impedance $\angle Z_o(j\omega)$ must be within $[-\pi/2, \pi/2]$, i.e., the real part of $Z_o(j\omega)$ is nonnegative.

For convenience, the requirement of the former is called as individual stability and the counterpart is named as output impedance passivity hereinafter.

B. Individual Stability

According to the Nyquist stability criterion, $Z = P - 2[N_{(+)} - N_{(-)}] = 0$ should be satisfied to ensure the individual stability, where Z and P denote the number of closed-loop and open-loop RHP poles, respectively, and $N_{(+)}$ and $N_{(-)}$ indicate the number of positive and negative $-\pi$ crossings, respectively.

As shown in (4), $T(s)$ contains no open-loop RHP poles, i.e., $P = 0$. Thus, $N_{(+)} - N_{(-)} = 0$ is required.

According to (4), the phase of the uncompensated loop gain is expressed as

$$\angle T(j\omega)|_{G_v(j\omega)=1} = \begin{cases} -1.5T_s\omega, \omega < \omega_r \\ -\pi - 1.5T_s\omega, \omega > \omega_r \end{cases} \tag{11}$$

which decreases monotonously, implying that $N_{(+)} = 0$. Since

$$-1.5\, T_s \times \omega_s/3 = -\pi, \tag{12}$$

$N_{(-)}$ might occur at $\omega_s/3$ or ω_r, as illustrated in Fig. 4. When $\omega_r \le \omega_s/3$, the negative crossing occurs at ω_r. Since the magnitude of $T(j\omega)$ at ω_r is ∞, the negative crossing is inevitable. Consequently, the system is doomed to instability. However, when $\omega_r > \omega_s/3$, the negative crossing occurs at $\omega_s/3$ and can be disabled by tuning G_v.

Recognizing that

$$\angle T(j\omega) = \angle G_v(j\omega) + \angle G_d(j\omega) + \begin{cases} 0, \omega < \omega_r \\ -\pi, \omega > \omega_r \end{cases} \tag{13}$$

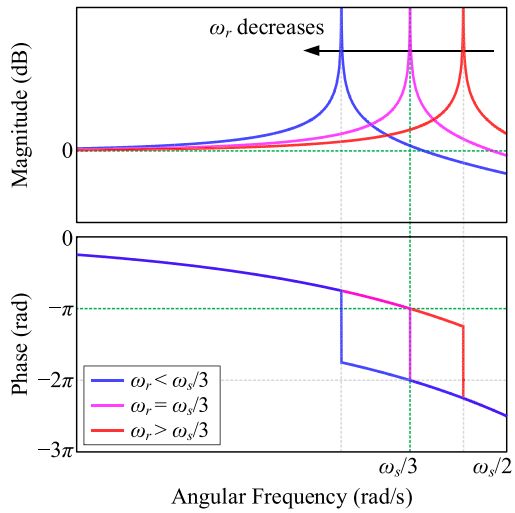

Fig. 4. Bode diagram of uncompensated loop gain under different ω_r.

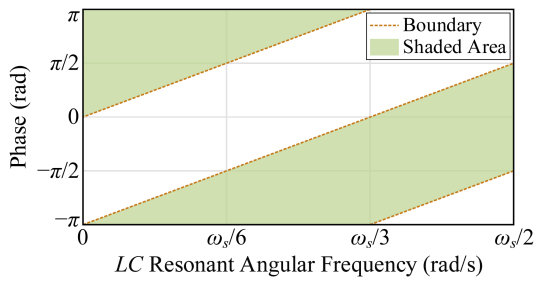

Fig. 5. Individual stability regions for voltage controller.

the system stability requires

$$\angle T\left(j\omega_r^-\right) \in \left(-2\pi + 2k\pi, -\pi + 2k\pi\right) \tag{14}$$

where k is an integer and, $\angle T\left(j\omega_r^-\right)$ denotes the left-hand limit of $\angle T(j\omega)$ at $\omega = \omega_r$, expressed as

$$\angle T\left(j\omega_r^-\right) = \lim_{\omega \to \omega_r^-} \angle T\left(j\omega\right) = \angle G_v\left(j\omega_r\right) - 3\pi\omega_r/\omega_s. \tag{15}$$

Substituting (15) into (14), yields

$$\angle G_v\left(j\omega_r\right) \in \left(3\pi\frac{\omega_r}{\omega_s} + 2k\pi, \pi + 3\pi\frac{\omega_r}{\omega_s} + 2k\pi\right). \tag{16}$$

According to (16), when ω_r varies from 0 to $\omega_s/2$, the satisfactory regions of $\angle G_v(j\omega_r)$ can be obtained, as shown in the shaded areas of Fig. 5. Here, considering that $\angle G_v(j\omega)$ generally does not exceed $[-\pi, \pi]$, only the satisfactory regions in $[-\pi, \pi]$, are presented. Notably, as long as $\angle G_v(j\omega_r)$ is in the shaded areas, the negative crossing at ω_r can be avoided.

C. Output Impedance Passivity

Recalling (8), the output impedance can be rewritten as

$$\begin{aligned} Z_o\left(s\right) &= \frac{Ls}{LCs^2 + G_v\left(s\right)G_d\left(s\right) + 1} \\ &= \frac{1}{Cs + \left[G_v\left(s\right)G_d\left(s\right) + 1\right]/Ls} \triangleq \frac{1}{Cs + 1/Z_{vp}\left(s\right)} \end{aligned} \tag{17}$$

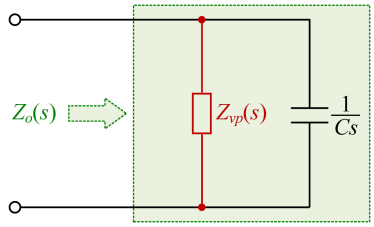

Fig. 6. Equivalent output impedance model of the GFM inverter.

where $Z_{vp}(s)$ represents the virtual parallel impedance introduced by the voltage controller and the time delay, expressed as

$$Z_{vp}\left(s\right) = \frac{Ls}{1 + G_v\left(s\right)G_d\left(s\right)}. \tag{18}$$

Accordingly, $Z_o(s)$ can be decomposed as a parallel connection of the filter capacitor C and the virtual parallel impedance $Z_{vp}(s)$, as shown in Fig. 6.

Since the filter capacitor is passive, the passivity of $Z_o(j\omega)$ only depends on the real part of $Z_{vp}(j\omega)$, i.e., $R_{vp}(j\omega)$. The sign of $R_{vp}(j\omega)$ is determined by

$$\operatorname{sgn}\left\{R_{vp}\left(j\omega\right)\right\} = \operatorname{sgn}\left\{\sin\left[\angle G_v\left(j\omega\right) + \angle G_d\left(j\omega\right)\right]\right\} \tag{19}$$

where $\operatorname{sgn}\{\cdot\}$ is the sign function.

Based on (19), in order to guarantee a nonnegative $R_{ac}(j\omega)$, the constraint on $\angle G_v(j\omega)$ can be derived as

$$\angle G_v\left(j\omega\right) \in \left[3\pi\frac{\omega}{\omega_s} + 2k\pi, \pi + 3\pi\frac{\omega}{\omega_s} + 2k\pi\right]. \tag{20}$$

The passive frequency range of $Z_o(j\omega)$ is exactly the range where $\angle G_v(j\omega)$ meets (20).

Comparing (20) with (16), it can be found that the phase constraint on output impedance passivity is identical with that on individual stability. Therefore, these two requirements can be unified into one for the GFM inverter with single-loop voltage control. For convenience, they will no longer be distinguished in the following.

D. Evaluation of Typical Single-Loop Voltage Controllers

Based on above analyses, the passivity properties of the GFM inverter with typical single-loop voltage controllers can be easily evaluated. Since the control scheme is implemented in the $\alpha\beta$ frame, the resonant part is commonly utilized in $G_v(s)$ to reduce the steady-state error [28], expressed as

$$R\left(s\right) = \frac{2\omega_i s}{s^2 + 2\omega_i s + \omega_o^2} \tag{21}$$

where $\omega_o = 2\pi f_o$ is the fundamental angular frequency, and ω_i is the bandwidth of the resonant part. In this article, ω_i is selected as π to guarantee enough gain of $R(s)$ when grid frequency fluctuates (such as, 49.5–50.5 Hz). Thus, in prior pieces of literature, the controllers with $R(s)$, such as PR [23], R [20], and R-PLF [24], are commonly employed.

Depicting the phase plots of PR, R, and R-PLF controllers in Fig. 5, yields Fig. 7. According to the phase constraint shown in (20), the passive ranges can be obtained.

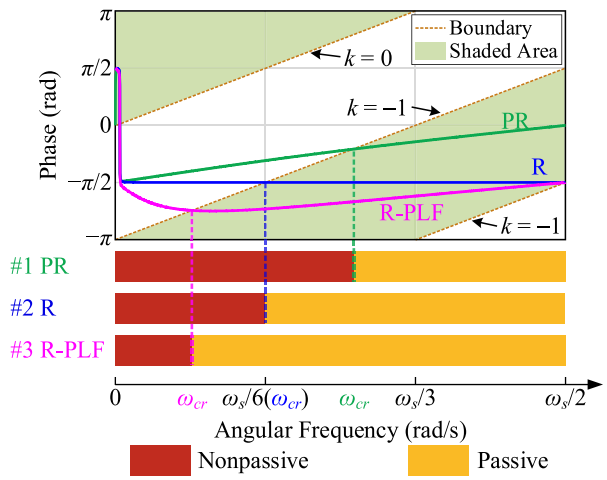

Fig. 7. Passive ranges of the GFM inverter with PR, R, and R-PLF voltage controllers.

As shown, compared to R controller, the proportional part of PR controller shrinks the passive range. This is because it reduces the phase lag of the resonant part, which agrees with the analysis in [20]. In contrast, PLF adds an additional phase lag, and thus widens the passive range. We can conclude that the phase lag of voltage controller benefits to the system passivation.

Once the frequencies of grid resonances fall within the non-passive ranges, the destabilization will occur, triggering protection or leading to physical damage [29]. It should be noticed that thanks to the phase lag of PLF, the system with R-PLF controller can be stable in the case of $f_r < f_s/6$, whereas PR and R controllers only stabilize the system in the case of $f_r > f_s/6$. Besides, no matter which voltage controller is adopted, the output impedance changes once from passive to nonpassive or vice versa in the entire frequency range. The critical angular frequency corresponding to this change is defined as $\omega_{cr} = 2\pi f_{cr}$, which is also remarked in Fig. 7. In order to prevent instability, the passivity enhancement method is required.

IV. Passivity Enhancement

A simple solution of passivity enhancement is introducing grid-current feedforward to reshape $Z_o(s)$. In this section, a generic grid-current feedforward scheme is explored for the GFM inverter with single-loop voltage control to eliminate its nonpassive frequency range.

A. Basic Idea

Fig. 8 shows the SISO control diagram after introducing the grid-current feedforward with a gain of $G_f(s)$. According to Fig. 8, the reshaped output impedance, denoted as $Z'_o(s)$, can be derived as

$$Z'_o(s) = -\frac{v_o(s)}{i_g(s)} = \frac{Ls + G_f(s)G_d(s)}{LCs^2 + G_v(s)G_d(s) + 1}. \quad (22)$$

By transformation, $Z'_o(s)$ can be decomposed as a parallel connection of the filter capacitor and a virtual parallel impedance

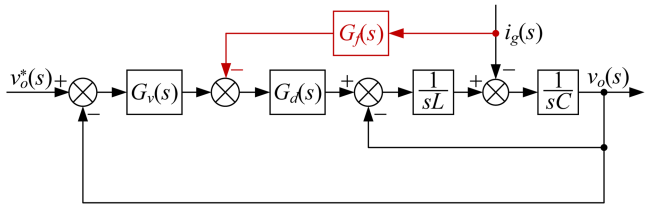

Fig. 8. SISO control block diagram of the GFM inverter with grid-current feedforward.

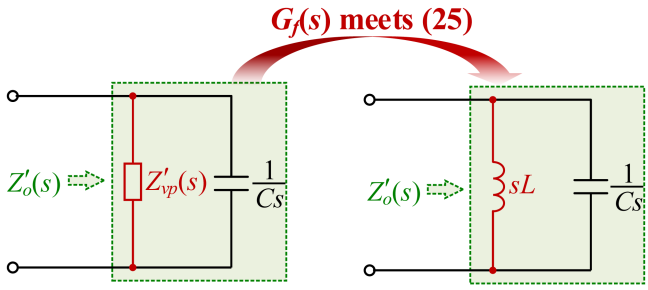

Fig. 9. Parallel equivalent model of the reshaped output impedance.

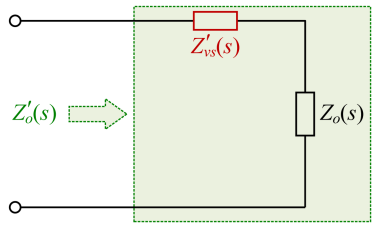

Fig. 10. Series equivalent model of the reshaped output impedance.

$Z'_{vp}(s)$, as shown in Fig. 9, where

$$Z'_{vp}(s) = \frac{Ls + G_f(s)G_d(s)}{1 + [G_v(s) - G_f(s)Cs]G_d(s)} = sL \cdot \frac{1 + G_f(s)G_d(s)/Ls}{1 + [G_v(s) - G_f(s)Cs]G_d(s)}. \quad (23)$$

It can be observed from (23) that, $Z'_{vp}(s)$ can be simplified as the pure inductance sL by letting

$$G_f(s)G_d(s)/Ls = [G_v(s) - G_f(s)Cs]G_d(s). \quad (24)$$

This can be achieved by selecting the feedforward function as

$$G_f(s) = \frac{LsG_v(s)}{LCs^2 + 1}. \quad (25)$$

In this way, the output impedance is reshaped as the parallel connection of the filter capacitor and the filter inductor, as shown in Fig. 9. Then, the system is naturally passive. However, the corresponding $G_f(s)$ contains a pure resonant item $1/(LCs^2+1)$, which may amplify high-frequency noise. To overcome this drawback, we attempt to find an alternative to replace this resonant item without introducing additional nonpassive ranges.

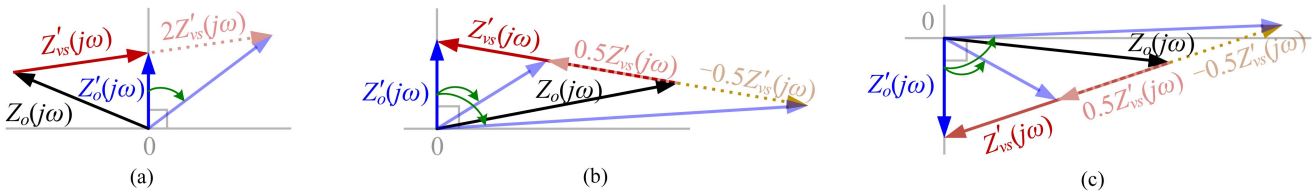

Fig. 11. Vector diagrams of $Z'_{vs}(j\omega)$ when (a) $\omega \in (0, \omega_{cr})$, (b) $\omega \in (\omega_{cr}, \omega_r]$, and (c) $\omega \in (\omega_r, \omega_s/2]$.

B. Feedforward Function

Combining (17) and (22), $Z'_o(s)$ can also be decomposed as a series connection of the original output impedance $Z_o(s)$ and a virtual series impedance $Z'_{vs}(s)$, as shown in Fig. 10, where

$$Z'_{vs}(s) = \frac{G_f(s)\,G_d(s)}{LCs^2 + G_v(s)\,G_d(s) + 1}. \tag{26}$$

Based on the phases of Z_o and Z'_o, the vector diagrams of $Z'_{vs} = Z'_o - Z_o$ in different frequency ranges can be obtained, as shown in Fig. 11(a)–(c). Observing Fig. 11, when we tune the length of the vector $\boldsymbol{Z'_{vs}}$ or reverse its direction, Z'_o can keep passive since it falls inside *Quadrant I* or *IV*. This observation is crucial for finding the alternative of the resonant item in feedforward function.

Substituing (25) into (26) and letting $s = j\omega$, the length of $\boldsymbol{Z'_{vs}(j\omega)}$ can be written as

$$|Z'_{vs}(j\omega)| = \left|\frac{1}{1 - LC\omega^2}\right| \cdot \left|\frac{\omega L G_v(j\omega) G_d(j\omega)}{-LC\omega^2 + G_v(j\omega)G_d(j\omega) + 1}\right|. \tag{27}$$

Notice that the resonant item $1/(1-LC\omega^2)$ can be regarded as a constant at a fixed frequency. Thus, we can use a constant m to replace it. According to (27) and Fig. 11, the requirements of m can be obtained as follows.

1) $\omega \in (0, \omega_{cr})$: The resonant item $1/(1-LC\omega^2)$ is positive. As shown in Fig. 11(a), the vector $\boldsymbol{Z'_{vs}}$ can be elongated along its orginal direction. According to (27), its length is directly proportional to that of the resonant item. Thus, $m > 1/(1-LC\omega^2)$ should be satisfied.
2) $\omega \in (\omega_{cr}, \omega_r)$: The resonant item $1/(1-LC\omega^2)$ is also positive. However, as shown in Fig. 11(b), the vector Z'_{vs} can be shorten or turned towards the opposite direction instead, corresponding to $0 < m < 1/(1-LC\omega^2)$ or $m < 0$.
3) $\omega \in (\omega_r, \omega_s/2)$: The resonant item $1/(1-LC\omega^2)$ is negative. As shown in Fig. 11(c), the vector Z'_{vs} can be shorten or turned toward the opposite direction, corresponding to $|m| < |1/(1-LC\omega^2)|$ or $m > 0$.

Based on the above requirements, the optional region of m can be obtained, as illustrated in the shaded area of Fig. 12. It is interesting that the line of $m = 1/(1 - LC\omega_{cr}^2)$ completely falls inside the shaded area. Therefore, the resonant item can be replaced by the positive constant $m = 1/(1 - LC\omega_{cr}^2)$. In order to verify its correctness, Fig. 13 depicts the Bode diagram of the reshaped output impedance. As shown, the passivity of output impedance is guaranteed in the entire frequency range.

However, since m is related to L and C which inevitably vary in practice, the passivity is vulnerable to the filter parameter fluctuations. As shown in Fig. 13, the nonpassive regions appear around ω_{cr} with $\pm 10\%$ fluctuations of L and C. Although these regions are not noticeable, they can still incur instability. Therefore, it is necessary to further enhance the robustness.

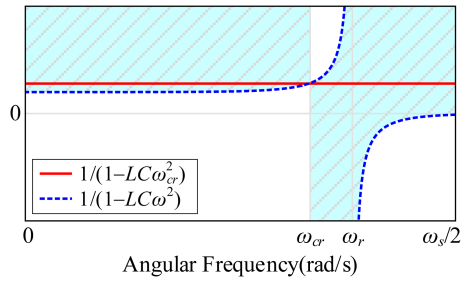

Fig. 12. Optional region of m that can replace the resonant item.

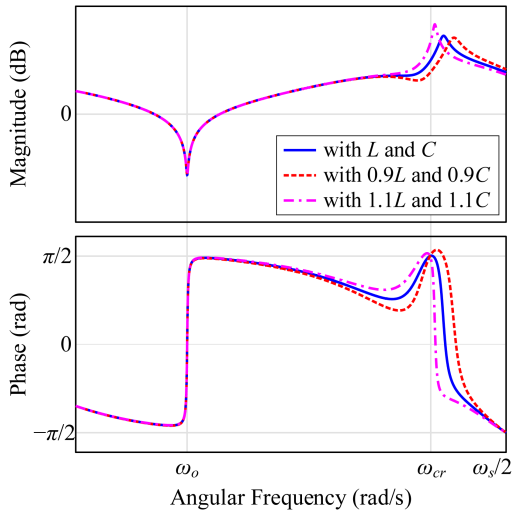

Fig. 13. Bode diagram of the reshaped output impedance when the resonant item of G_f is replaced by $m = 1/(1 - LC\omega_{cr}^2)$.

C. Robustness Enhancement

To enhance the robustness against the filter parameter fluctuation, a proper phase compensation at the critical frequency ω_{cr} is perferable to secure a certain margin of Z'_o to the line of $\pi/2$. Fig. 14 plots the vector diagram of uncompensated Z'_{vs}, Z_o, and Z'_o at ω_{cr}. Notice that the uncompensated $\angle Z'_{vs}(j\omega_{cr})$ is $-\pi/2$ (which is theoretically proved in Appendix). A simple idea to achieve the target comes up, which is to tune $\angle Z'_{vs}(j\omega_{cr})$ with a phase-lead compensator G_c. Accordingly, the vector $Z'_o(j\omega_{cr})$ synthesized by $Z'_{vs}(j\omega_{cr})$ and $Z_o(j\omega_{cr})$ will fall into *Quadrant I*, and thus the margin of Z'_o will be ensured. The expression of $G_c(s)$ is

$$G_c(s) = \frac{1 + \alpha_{\text{lead}}\tau_{\text{lead}}s}{1 + \tau_{\text{lead}}s} \tag{28}$$

TABLE I
STABILITY ANALYSIS AND PASSIVITY DESIGN FOR DIFFERENT VOLTAGE CONTROLLERS

Type	Transfer Function of Voltage Controller $G_v(s)$		Individually Stable Range	Output Impedance Passive Range	Voltage Controller Approximation	Transfer Function of Feedforward Controller $G_f(s)$	
I	PR	$K_{pv}+K_{rv}R(s)$	$(\omega_{cr1}, \omega_s/2]$ $\omega_{cr1} \in (\omega_s/6, \omega_s/3)$	$[\omega_{cr1}, \omega_s/2]$	$K_{pv}+K_{rv}2\omega_i/s$	PD-Lead	$\frac{L\left(K_{pv}+K_{rv}2\omega_i s\right)}{1-LC\omega_{cr1}^2}\cdot\frac{1+\alpha_{\text{lead}}\tau_{\text{lead}}s}{1+\tau_{\text{lead}}s}$
II	R[20], [27]	$K_{rv}R(s)$	$(\omega_{cr2}, \omega_s/2)$ $\omega_{cr2}=\omega_s/6$	$[\omega_{cr2}, \omega_s/2]$	$K_{rv}2\omega_i/s$	Lead	$\frac{LK_{rv}2\omega_i}{1-LC\omega_{cr2}^2}\cdot\frac{1+\alpha_{\text{lead}}\tau_{\text{lead}}s}{1+\tau_{\text{lead}}s}$
	IR[20]	$K_{iv}/s+K_{rv}R(s)$			$\left(K_{iv}+K_{rv}2\omega_i\right)/s$		$\frac{L\left(K_{iv}+K_{rv}2\omega_i\right)}{1-LC\omega_{cr2}^2}\cdot\frac{1+\alpha_{\text{lead}}\tau_{\text{lead}}s}{1+\tau_{\text{lead}}s}$
III	R-PLF[22]	$K_{rv}R(s)\cdot\frac{1+bTs}{1+Ts}$	$(\omega_{cr3}, \omega_s/2)$ $\omega_{cr3} \in (\omega_o, \omega_s/6)$	$[\omega_{cr3}, \omega_s/2]$	$K_{rv}2\omega_i\frac{1+bTs}{s(1+Ts)}$	PLF-Lead	$\frac{LK_{rv}2\omega_i}{1-LC\omega_{cr3}^2}\cdot\frac{1+bTs}{1+Ts}\cdot\frac{1+\alpha_{\text{lead}}\tau_{\text{lead}}s}{1+\tau_{\text{lead}}s}$

[Note: (1) ω_{cr1} and ω_{cr3} are related to the parameters of voltage controllers. (2) in type III, $b<1$.]

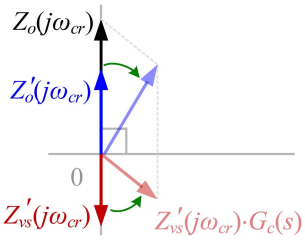

Fig. 14. Vector diagram of $Z'_{vs}(j\omega)$ at ω_{cr}.

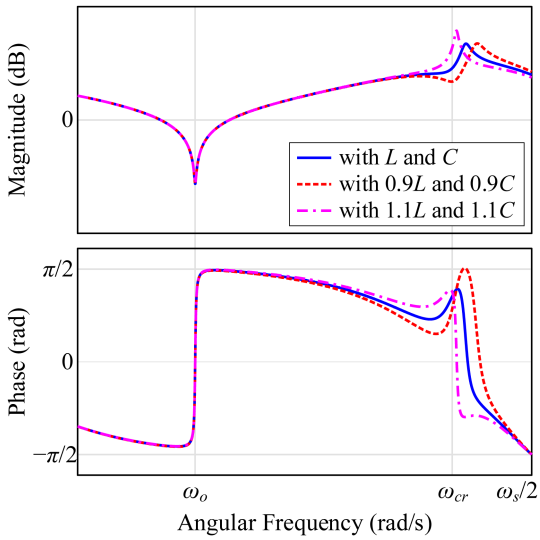

Fig. 15. Bode diagram of the reshaped output impedance with the feedforward function given in (30).

where

$$\begin{cases}\alpha_{\text{lead}}=\frac{1+\sin\varphi_{m\_\text{lead}}}{1-\sin\varphi_{m\_\text{lead}}}\\ \tau_{\text{lead}}=\frac{1}{\omega_{m\_\text{lead}}\sqrt{\alpha_{\text{lead}}}}\end{cases}. \tag{29}$$

Therefore, the feedforward function should be adjusted as

$$G_f(s)=\frac{LsG_v(s)}{1-LC\omega_{cr}^2}\cdot\frac{1+\alpha_{\text{lead}}\tau_{\text{lead}}s}{1+\tau_{\text{lead}}s}. \tag{30}$$

The Bode diagram of $Z'_o(s)$ with this feedforward function is plotted in Fig. 15. As shown, $Z'_o(s)$ is passive even with the fluctuation of LC filter paramters. The feedforward functions for the common-used voltage controllers are given in Table I, where, as a rule of thumb, $R(s)\approx 2\omega_i/s$ [23] is considered to simplify $G_f(s)$. Note that the proposed grid-current feedforward scheme is also suitable for the single-loop voltage controllers in the dq frame.

TABLE II
SYSTEM PARAMETERS

Parameter	Value	Parameter	Value
DC-link voltage V_{dc}	700V	Fundamental frequency f_o	50Hz
Grid voltage V_g (RMS)	220V	Filter inductor L	1.5mH
Rated power S_n	6kVA	Filter capacitor C	3.3μF
Switching frequency f_{sw}	10kHz	Sampling frequency f_s	10kHz

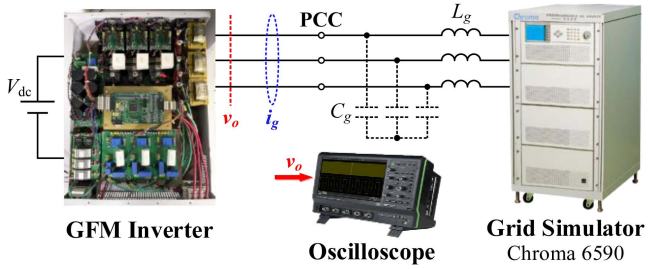

Fig. 16. Configuration of the experimental setup.

D. Design Procedure

Based on the above analysis, the design procedure can be concluded, which is elaborated as follows.

1) Given the desired filter parameters, the type of voltage controller, such as PR, R, R-PLF, can be determined according to the individually stable range in Table I.
2) Based on the specifications of the loop gain including the steady state error, crossover frequency f_c, phase margin (PM) and gain margin (GM), select the voltage controller parameters [23].

TABLE III
PARAMETERS AND DISCRETIZATION METHODS OF THE CONTROLLERS

Voltage Controller				Feedforward Controller			
Type	Parameters		Discretization Method	Type	Parameters		Discretization Method
PR	K_{pv}	0.03	Tustin with prewarping	PD-Lead	ω_{cr1}	$2\pi\times1.85$ krad/s	PD：Backward-lead [30] Lead：Tustin
	K_{rv}	370			φ_{m_lead}	$\pi/18$	
R	K_{rv}	480	Tustin with prewarping	Lead	ω_{cr2}	$2\pi\times1.67$ krad/s	Tustin
					φ_{m_lead}	$\pi/18$	
R-PLF	K_{rv}	550	R: Tustin with prewarping PLF: Tustin	PLF-Lead	ω_{cr3}	$2\pi\times1.19$ krad/s	PLF：Tustin Lead：Tustin
	b	0.33			φ_{m_lead}	$\pi/30$	
	T	1.22×10^{-4}					

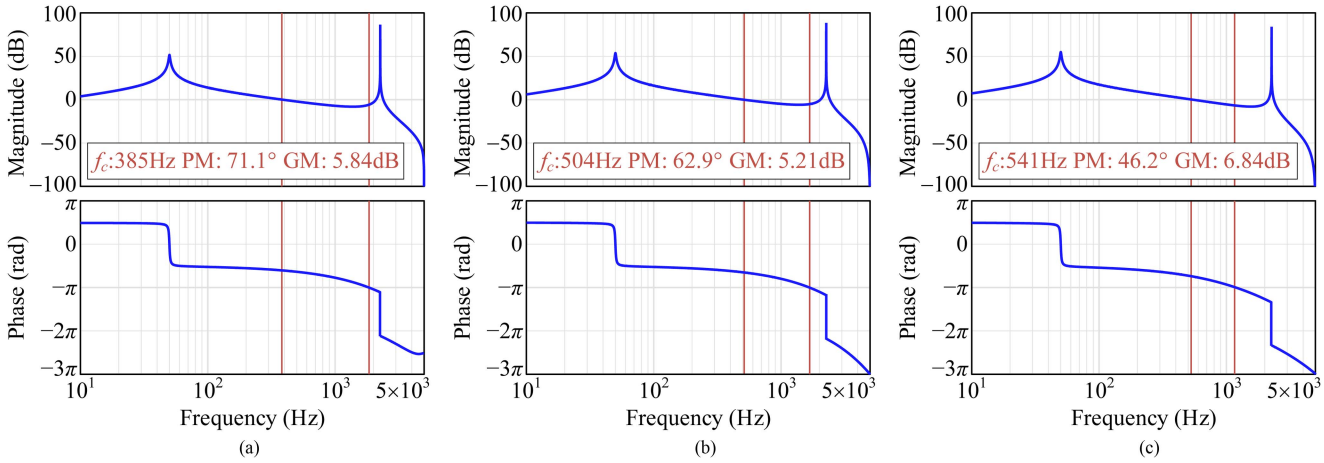

Fig. 17. Bode diagrams of the loop gain with different voltage controllers. (a) PR controller. (b) R controller. (c) R-PLF controller.

3) By drawing the passive range graph like Fig. 7, obtain the critical angular frequency ω_{cr} when the passivity property of output impedance changes.
4) Setting $\omega_{m\_\mathrm{lead}} = \omega_{cr}$ and initializing a compensation phase $\varphi_{m\_\mathrm{lead}}$, the phase-lead compensation parameters α_{lead} and τ_{lead} will be solved from (29).
5) Based on $R(s) \approx 2\omega_i/s$, the approximation of the specific voltage controller can be obtained. Substitute the filter inductor parameter L, the determined ω_{cr}, and the approximation of $G_v(s)$ into (30), yielding the expression of the grid-current feedforward controller.
6) Plot the phase curve of $Z'_o(s)$. If there exists the nonpassive region, the phase-lead compensation is inadequate. Then, adjust $\varphi_{m\_\mathrm{lead}}$ and iterate the above design procedure, until a passive $Z'_o(s)$ is obtained.

V. VERIFICATION

A 6-kVA prototype with the key parameters listed in Table II was built in the laboratory. The configuration of the experimental setup is presented in Fig. 16. The three-phase inverter bridges are implemented with three IGBT modules (CM200DY-24NF), which are driven by M57962L. The control algorithm is implemented in a TI TMS320F2812 DSP. The ideal grid voltage v_g is simulated by a programmable ac source (Chroma 6590), and the grid impedance $L_g - C_g$ is emulated by the external inductor and capacitor.

Here, three different voltage controllers [PR, R, and R-PLF] are utilized to confirm the effectiveness and generality of the proposed grid-current feedforward scheme. Following the above design procedure, the parameters of those voltage controllers and the corresponding grid-current feedforward controllers can be obtained, which are given in Table III.

According to the passivity-based stability criterion, the individual stability and the output impedance passivity must be satisfied simultaneously. The Bode diagrams of their loop gains are firstly depicted to check the individual stability, as shown in Fig. 17. It can be observed that those systems are stable with sufficient bandwidth, PM and GM. Based on the above parameters, the output impedance in case of the rated LC filter parameters and the grid impedance are plotted in Fig. 18. Therein, $Z_{g1}(s)$ and $Z_{g2}(s)$ represent the traditionally inductive grid impedance and the equivalent LC resonant grid impedance in the scenario where there exists power factor correction capacitor at the PCC [31], respectively. It can be seen that without $G_f(s)$, the nonpassivity of $Z_o(s)$ makes the phase difference between $Z_o(s)$ and $Z_{g2}(s)$ exceed π at their magnitude intersection frequency f_{int}. Referring to the impedance stability criterion, it leads to instability.

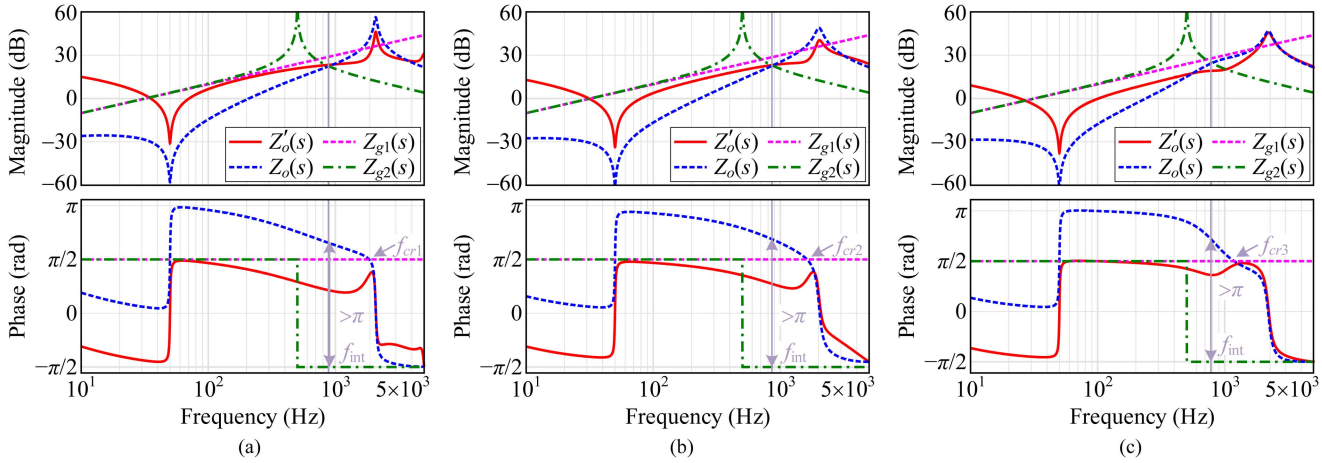

Fig. 18. Bode diagrams of the output impedance with different voltage controllers in case of the rated *LC* filter parameters. (a) PR controller. (b) R controller. (c) R-PLF controller.

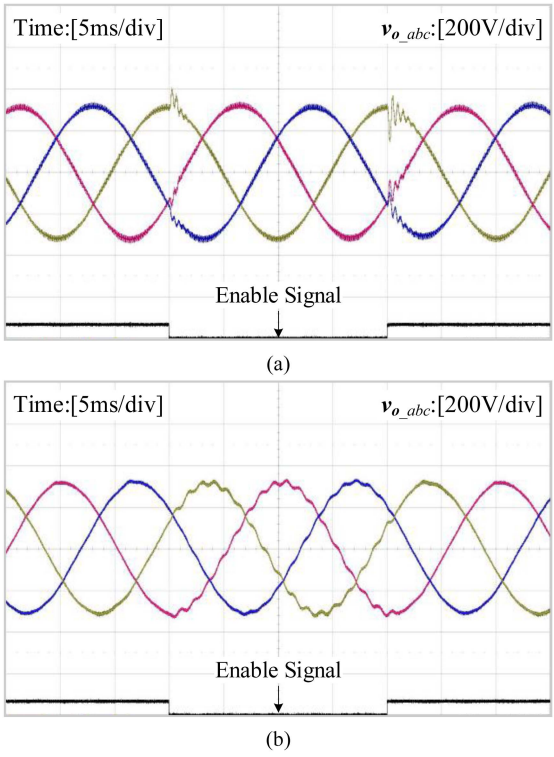

Fig. 19. Experimental results with PR controller in case of the rated *LC* filter parameters, where the feedforward controller is enabled when the enable signal is high, and disabled when the enable signal is low. (a) Grid impedance is purely inductive. (b) Grid impedance is inductive in the low-frequency range but capacitive in the high-frequency range.

On the contrary, the nonpassive range can be eliminated till $f_s/2$ by the proposed grid-current feedforward control, and thus the system is stable.

The following experiments were further conducted to confirm the correctness of the above passivity analysis.

The first set of experiments were conducted to confirm the theoretical analysis with PR controller. Fig. 19(a) shows the tested experimental result with the inductive grid impedance [L_g = 5 mH]. Therein, the feedforward controller is removed at the falling edge of the enable signal, and recovered at the rising edge. As shown, the measured output voltages $\boldsymbol{v}_{o\_abc}$ are all stable no matter with the feedforward controller or not. Fig. 19(b) shows the result with the *LC* resonant grid impedance [$L_g = 5$ mH; $C_g = 20$ μF]. As shown, the oscillations arise in all the measured output voltages when the feedforward controller is disabled. Then, the oscillations decay rapidly and $\boldsymbol{v}_{o\_abc}$ finally become stable after the feedforward controller reintroduces.

The second set of experiments were carried out to confirm the theoretical analysis with R controller. Fig. 20(a) shows the tested experimental result with the inductive grid impedance [L_g = 5 mH], and Fig. 20(b) shows the result with the *LC* resonant grid impedance [$L_g = 5$ mH and $C_g = 20$ μF]. Similarly, the feedforward controller is removed at the falling edge of the enable signal and recovered at the rising edge. It can be observed in Fig. 20(a) that, the measured signals $\boldsymbol{v}_{o\_abc}$ can remain stable even though the feedforward controller is disabled. In contrast, all the measured output voltages tend to oscillate without the feedforward controller, as shown in Fig. 20(b).

The third set of experiments were conducted to confirm the theoretical analysis with R-PLF controller. Fig. 21 shows the experimental results, where the feedforward controller is removed at the falling edge of the enable signal and recovered at its rising edge. As shown in Fig. 21(a), the measured $\boldsymbol{v}_{o\_abc}$ are all stable, meaning the feedforward controller is not required in the case of inductive grid impedance. Yet, as shown in Fig. 21(b), under capacitive grid condition, the feedforward controller is necessary to ensure the system stability.

These results agree with the theoretical expectations and have confirmed that the proposed grid-current feedforward scheme can effectively enhance the passivity property of the GFM inverter with single-loop voltage control.

The last set of experiments were conducted to verify the robustness against the filter parameter fluctuations. Here, we take the GFM inverter with R controller as an example. Fig. 22 shows the corresponding experimental result with ±10% fluctuations of both *L* and *C*. To show the effectiveness and necessity of

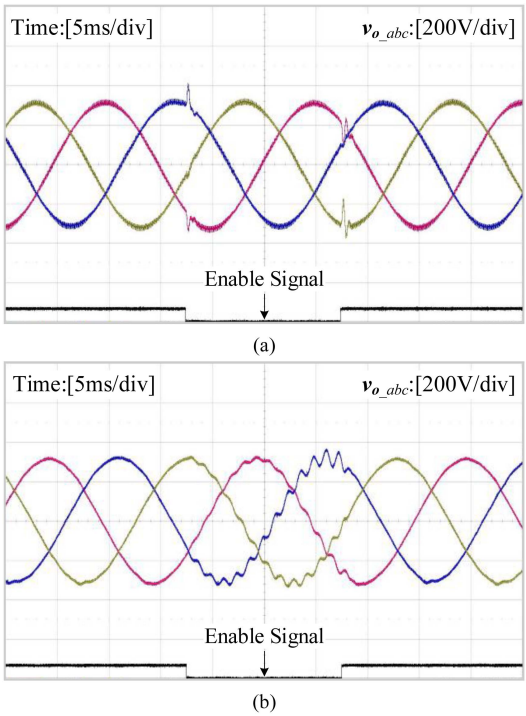

Fig. 20. Experimental results with R controller in case of the rated *LC* filter parameters, where the feedforward controller is enabled when the enable signal is high, and disabled when the enable signal is low. (a) Grid impedance is purely inductive. (b) Grid impedance is inductive in the low-frequency range but capacitive in the high-frequency range.

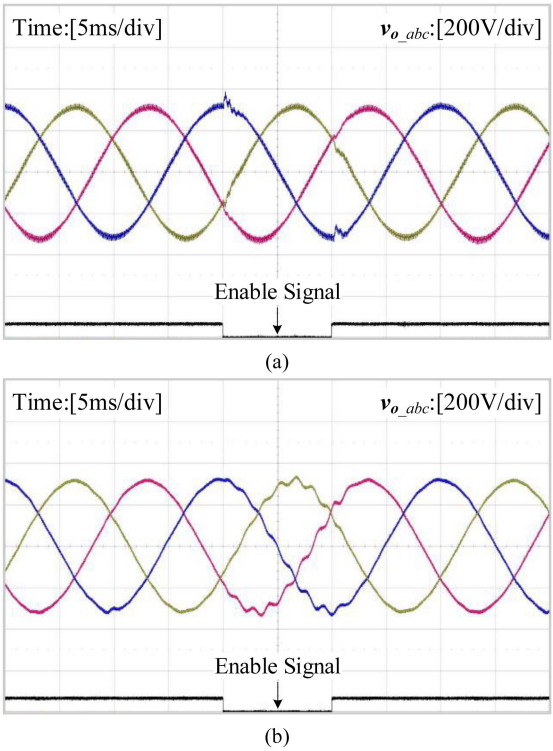

Fig. 21. Experimental results with R-PLF controller in case of the rated *LC* filter parameters, where the feedforward controller is enabled when the enable signal is high, and disabled when the enable signal is low. (a) Grid impedance is purely inductive. (b) Grid impedance is inductive in the low-frequency range but capacitive in the high-frequency range.

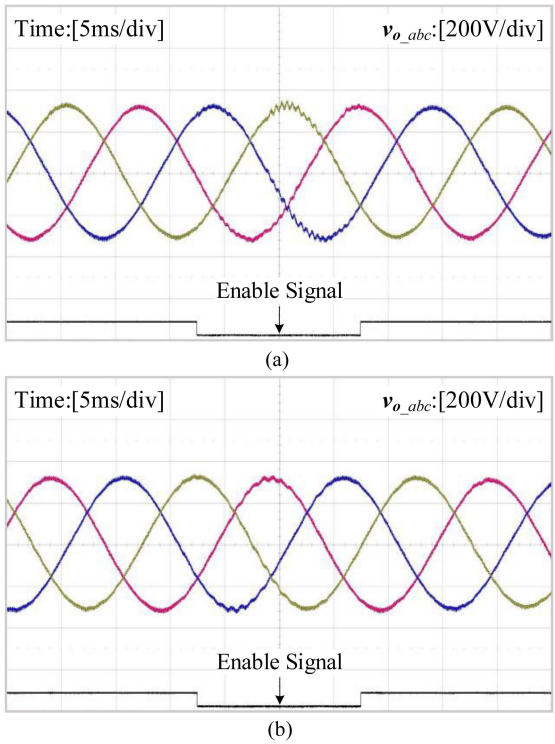

Fig. 22. Experimental results with R controller in case of $+/-10\%$ *LC* filter parameters tolerance, where the lead compensator in the feedforward controller is enabled where the enable signal is high, and disabled when the enable signal is low. (a) -10% *LC* filter parameters tolerance. (b) $+10\%$ *LC* filter parameters tolerance.

the phase-lead compensator in the feedforward controller, the compensator is disabled at the falling edge of the enable signal and recovered at the rising edge. As shown, the oscillations arise in the measured $\boldsymbol{v}_{o\_abc}$ when the compensator is disabled; when the compensator is enabled, oscillation decays rapidly and the output voltage tends to be stable. The results confirm that the proposed grid-current feedforward scheme is effective and robust to the *LC* filter parameter fluctuation.

VI. Conclusion

Focusing on the GFM inverter with single-loop voltage control, this article first reveals, the phase constraints of individual stability and output impedance passivity on the voltage controller are identical. This finding bridges the linkage between the two indices of passivity and provides a novel perspective to understand its concept. On its basis, the passivity properties of the GFM inverter with typical voltage controllers are evaluated. It points out that the phase lag of the voltage controller benefits to the system passivation. In order to eliminate the unexpected nonpassive frequency ranges, a generic grid-current feedforward scheme is proposed, which extends the passive range up to the Nyquist frequency and is robust to the filter parameter fluctuation. A simple parameter tuning process, compatible with various voltage controllers, is also provided. Finally, experiments conducted on a 6-kVA prototype confirm the effectiveness and robustness of the proposed grid-current feedforward scheme.

APPENDIX

The uncompensated $\angle Z'_{vs}(j\omega_{cr})$ is derived in this appendix. Combining (17) and (26), yields

$$Z'_{vs}(s) = Z_o(s) \cdot \frac{G_v(s)\, G_d(s)}{1 - LC\omega_{cr}^2}. \tag{A1}$$

Thus, these exists

$$\angle Z'_{vs}(j\omega_{cr}) = \angle Z_o(j\omega_{cr}) + \angle G_v(j\omega_{cr}) + \angle G_d(j\omega_{cr}). \tag{A2}$$

According to Fig. 7, we have

$$\begin{aligned} \angle G_v(j\omega_{cr}) &= \pi + 3\pi\omega_{cr}/\omega_s + 2\pi \times (-1) \\ &= 3\pi\omega_{cr}/\omega_s - \pi. \end{aligned} \tag{A3}$$

Considering $\angle Z_o(j\omega_{cr}) = \pi/2$ and $\angle G_d(j\omega_{cr}) = -3\pi\omega_{cr}/\omega_s$, (A2) can be written as

$$\begin{aligned} \angle Z'_{vs}(j\omega_{cr}) &= \pi/2 + 3\pi\omega_{cr}/\omega_s - \pi - 3\pi\omega_{cr}/\omega \\ &= -\pi/2. \end{aligned} \tag{A4}$$

REFERENCES

[1] J. Rocabert, A. Luna, F. Blaabjerg, and P. Rodríguez, "Control of power converters in AC microgrids," *IEEE Trans. Power Electron.*, vol. 27, no. 11, pp. 4734–4749, Nov. 2012.

[2] X. Ruan, X. Wang, D. Pan, D. Yang, W. Li, and C. Bao, *Control Techniques for LCL-Type Grid-Connected Inverters*. Berlin, Germany: Springer, 2017.

[3] Y. He, X. Wang, X. Ruan, D. Pan, and K. Qin, "Hybrid active damping combining capacitor current feedback and point of common coupling voltage feedforward for *LCL*-type grid-connected inverter," *IEEE Trans. Power Electron.*, vol. 36, no. 2, pp. 2373–2383, Feb. 2021.

[4] D. Pan, X. Ruan, C. Bao, W. Li, and X. Wang, "Optimized controller design for *LCL*-type grid-connected inverter to achieve high robustness against grid-impedance variation," *IEEE Trans. Ind. Electron.*, vol. 62, no. 3, pp. 1537–1547, Mar. 2015.

[5] X. Wang, M. G. Taul, H. Wu, Y. Liao, F. Blaabjerg, and L. Harnefors, "Grid-synchronization stability of converter-based resources—an overview," *IEEE Open J. Ind. Appl.*, vol. 1, pp. 115–134, 2020.

[6] R. H. Lasseter, Z. Chen, and D. Pattabiraman, "Grid-forming inverters: A critical asset for the power grid," *IEEE J. Emerg. Sel. Top. Power Electron.*, vol. 8, no. 2, pp. 925–935, Jun. 2020.

[7] H. Wu and X. Wang, "Small-signal modeling and controller parameters tuning of grid-forming VSCs with adaptive virtual impedance-based current limitation," *IEEE Trans. Power Electron.*, vol. 37, no. 6, pp. 7185–7199, Jun. 2022.

[8] X. Wang and F. Blaabjerg, "Harmonic stability in power electronic-based power systems: Concept, modeling, and analysis," *IEEE Trans Smart Grid*, vol. 10, no. 3, pp. 2858–2870, May 2019.

[9] D. Yang and X. Wang, "Unified modular state-space modeling of grid-connected voltage-source converters," *IEEE Trans. Power Electron.*, vol. 35, no. 9, pp. 9700–9715, Sep. 2020.

[10] J. Sun, "Impedance-based stability criterion for grid-connected inverters," *IEEE Trans. Power Electron*, vol. 26, no. 11, pp. 3075–3078, Nov. 2011.

[11] W. Cao, Y. Ma, L. Yang, F. Wang, and L. M. Tolbert, "D–Q impedance based stability analysis and parameter design of three-phase inverter-based AC power systems," *IEEE Trans. Ind. Electron.*, vol. 64, no. 7, pp. 6017–6028, Jul. 2017.

[12] W. Cao, Y. Ma, and F. Wang, "Sequence-impedance-based harmonic stability analysis and controller parameter design of three-phase inverter-based multibus AC power systems," *IEEE Trans. Power Electron.*, vol. 32, no. 10, pp. 7674–7693, Oct. 2017.

[13] L. Harnefors, L. Zhang, and M. Bongiorno, "Frequency-domain passivity-based current controller design," *IET Power Electron.*, vol. 1, no. 4, pp. 455–465, Nov. 2008.

[14] L. Harnefors, X. Wang, A. G. Yepes, and F. Blaabjerg, "Passivity-based stability assessment of grid-connected VSCs—an overview," *IEEE J. Emerg. Sel. Top. Power Electron.*, vol. 4, no. 1, pp. 116–125, Mar. 2016.

[15] X. Wang, Y. He, D. Pan, H. Zhang, Y. Ma, and X. Ruan, "Passivity enhancement for *LCL*-filtered inverter with grid current control and capacitor current active damping," *IEEE Trans. Power Electron.*, vol. 37, no. 4, pp. 3801–3812, Apr. 2022.

[16] H. Wu and X. Wang, "Virtual-flux-based passivation of current control for grid-connected VSCs," *IEEE Trans. Power Electron.*, vol. 35, no. 12, pp. 12673–12677, Dec. 2020.

[17] L. Harnefors, R. Finger, X. Wang, H. Bai, and F. Blaabjerg, "VSC input-admittance modeling and analysis above the nyquist frequency for passivity-based stability assessment," *IEEE Trans. Ind. Electron.*, vol. 64, no. 8, pp. 6362–6370, Aug. 2017.

[18] C. Xie, K. Li, J. Zou, and J. M. Guerrero, "Passivity-based stabilization of *LCL*-type grid-connected inverters via a general admittance model," *IEEE Trans. Power Electron.*, vol. 35, no. 6, pp. 6636–6648, Jun. 2020.

[19] A. Akhavan, S. Golestan, J. C. Vasquez, and J. M. Guerrero, "Passivity enhancement of voltage-controlled inverters in grid-connected microgrids considering negative aspects of control delay and grid impedance variations," *IEEE J. Emerg. Sel. Top. Power Electron.*, vol. 9, no. 6, pp. 6637–6649, Dec. 2021.

[20] Y. Liao, X. Wang, and F. Blaabjerg, "Passivity-based analysis and design of linear voltage controllers for voltage-source converters," *IEEE Open J. Ind. Electron. Soc.*, vol. 1, pp. 114–126, 2020.

[21] W. Cao, Y. Ma, and F. Wang, "Adaptive impedance compensation of inverters for stable grid integration based on online resonance detection," in *Proc. IEEE Appl. Power Electron. Conf. Expo.*, 2019, pp. 3151–3158.

[22] Y. Geng, Y. Yun, R. Chen, K. Wang, H. Bai, and X. Wu, "Parameters design and optimization for *LC*-type off-grid inverters with inductor-current feedback active damping," *IEEE Trans. Power Electron.*, vol. 33, no. 1, pp. 703–715, Jan. 2018.

[23] X. Chen, X. Ruan, D. Yang, H. Wu, and W. Zhao, "Step-by-step controller design of voltage closed-loop control for virtual synchronous generator," in *Proc. IEEE Energy Conver. Congr. Expo.*, 2015, pp. 3760–3765.

[24] X. Wang, P. C. Loh, and F. Blaabjerg, "Stability analysis and controller synthesis for single-loop voltage-controlled vsis," *IEEE Trans. Power Electron.*, vol. 32, no. 9, pp. 7394–7404, Sep. 2017.

[25] H. Akagi, E. Watanabe, and M. Aredes, *Instantaneous Power Theory and Applications to Power Conditioning*. Piscataway, NJ, USA: IEEE Press, 2007.

[26] Y. Ma, W. Cao, L. Yang, F. Wang, and L. M. Tolbert, "Virtual synchronous generator control of full converter wind turbines with short-term energy storage," *IEEE Trans. Ind. Electron.*, vol. 64, no. 11, pp. 8821–8831, Nov. 2017.

[27] D. Pan, X. Wang, F. Liu, and R. Shi, "Transient stability of voltage-source converters with grid-forming control: A design-oriented study," *IEEE J. Emerg. Sel. Top. Power Electron.*, vol. 8, no. 2, pp. 1019–1033, Jun. 2020.

[28] E. Twining and D. G. Holmes, "Grid current regulation of a three-phase voltage source inverter with an *LCL* input filter," *IEEE Trans. Power Electron.*, vol. 18, no. 3, pp. 888–895, May 2003.

[29] C. Zou et al., "Analysis of resonance between a VSC-HVDC converter and the AC grid," *IEEE Trans Power Electron.*, vol. 33, no. 12, pp. 10157–10168, Dec. 2018.

[30] D. Pan, X. Ruan, and X. Wang, "Direct realization of digital differentiators in discrete domain for active damping of *LCL*-type grid-connected inverter," *IEEE Trans. Power Electron.*, vol. 33, no. 10, pp. 8461–8473, Oct. 2018.

[31] X. Wang, F. Blaabjerg, M. Liserre, Z. Chen, J. He, and Y. Li, "An active damper for stabilizing power-electronics-based AC systems," *IEEE Trans. Power Electron.*, vol. 29, no. 7, pp. 3318–3329, Jul. 2014.

Guotao Wu (Student Member, IEEE) received the B.S. degree from Northwest A&F University, Yangling, China, in 2019, and the M.S. degree from Huazhong University of Science and Technology, Wuhan, China, in 2022, both in electrical engineering.

He is currently a R&D Assistant Power Electronics Engineer with ABB Engineering (Shanghai) Ltd, Shanghai, China. His research interests include modeling and control of grid-connected converters, harmonics analysis and control, and stability of renewable energy generation system.

Yuying He (Member, IEEE) received the B.S. degree from Central South University, Changsha, China, in 2015, and the Ph.D. degree from Huazhong University of Science and Technology, Wuhan, China, in 2022, both in electrical engineering.

From May 2021 to May 2022, she was also with E. ON Energy Research Center, RWTH Aachen University, Aachen, Germany. Since June 2022, she has been a tenure-track Associate Professor with Hohai University, Nanjing, China. Her research interests include modeling and control of grid-connected converters, harmonics analysis and control, and stability of renewable energy generation system.

Hao Zhang (Student Member, IEEE) received the B.S. degree in electrical engineering from Chongqing University, Chongqing, China, in 2020. He is currently working toward the M.S. degree in electrical engineering, Huazhong University of Science and Technology, Wuhan, China.

His research interests include modeling and control of grid-connected converters, harmonics analysis and control, and stability of renewable energy generation system.

Xuehua Wang (Member, IEEE) received the B.S. degree from Nanjing University of Technology, Nanjing, China, in 2001, and the M.S. and Ph.D. degrees from Nanjing University of Aeronautics and Astronautics, Nanjing, China, in 2004 and 2008, respectively, all in electrical engineering.

Since 2008, he has been with Huazhong University of Science and Technology, China, where he was a Postdoctoral Fellow, from 2008 to 2011 and is an Associate Professor currently with the School of Electrical and Electronic Engineering. His main research interests include multilevel inverter and renewable energy generation system.

Donghua Pan (Member, IEEE) received the B.S. and Ph.D. degrees in electrical engineering from Huazhong University of Science and Technology, Wuhan, China, in 2010 and 2015, respectively.

From July 2015 to August 2017, he was a Research Engineer with Inovance Technology Co., Ltd., Suzhou, China. From September 2017 to October 2019, he was a Postdoctoral Fellow with the Department of Energy Technology, Aalborg University, Aalborg, Denmark. From November 2019 to December 2021, he was a Senior Manager with a holding company of China State Shipbuilding Corporation, Wuhan, China. Since January 2022, he has been the Head of GoodWe Technologies Co., Ltd. Wuhan Branch, Wuhan, China. He has authored or coauthored more than 40 peer-reviewed technical papers and a book *Control Techniques for LCL-type Grid-connected Inverters* (Springer, 2018). His research interests include magnetic integration techniques, modeling and control of grid-connected converters, and wide bandgap power conversion systems.

Dr. Pan was the recipient of the Outstanding Reviewer Award of IEEE TRANSACTIONS ON POWER ELECTRONICS in 2017 and 2021, the Best Paper Award at 2018 IEEE 4th Southern Power Electronics Conference, and the World's Top 2% Scientists by Stanford University in 2020–2021.

Xinbo Ruan (Fellow, IEEE) received the B.S. and Ph.D. degrees in electrical engineering from Nanjing University of Aeronautics and Astronautics (NUAA), Nanjing, China, in 1991 and 1996, respectively.

In 1996, he was with the Faculty of Electrical Engineering Teaching and Research Division, NUAA, where he was a Professor with the College of Automation Engineering in 2002 and has been engaged in teaching and research in the field of power electronics. From August to October 2007, he was a Research Fellow with the Department of Electronic and Information Engineering, Hong Kong Polytechnic University, Hong Kong. From March 2008 to August 2011, he was with the School of Electrical and Electronic Engineering, Huazhong University of Science and Technology. He is the author or co-author of 13 books and more than 300 technical papers published in journals and conferences. His main research interests include resonant and soft-switching power converters, power converter topologies and control, grid-connected converters and system for renewable energy, modeling and stability of power converters, and envelop tracking power supply.

Dr. Ruan was a recipient of Sustainable Energy Systems Technical Achievement Award from IEEE Power Electronics Society in 2022, the Delta Scholarship by the Delta Environment and Education Fund in 2003 and was a recipient of the Special Appointed Professor of the Chang Jiang Scholars Program by the Ministry of Education, China, in 2007. From 2005 to 2013, and since 2017, he has been the Vice President of the China Power Supply Society. From 2014 to 2016, he was the Vice Chair of the Technical Committee on Renewable Energy Systems within the IEEE Industrial Electronics Society. He is currently an Editor for IEEE JOURNAL OF EMERGING AND SELECTED TOPICS ON POWER ELECTRONICS, and an Associate Editor for IEEE TRANSACTIONS ON INDUSTRIAL ELECTRONICS, IEEE TRANSACTIONS ON POWER ELECTRONICS, IEEE TRANSACTIONS ON CIRCUITS AND SYSTEMS—II. He was the General Chair of 2020 IEEE 9th International Power Electronics and Motion Control Conference and the General Secretary of 2016 IEEE 8th International Power Electronics and Motion Control Conference, a Technical Program Committee Chair of the IEEE 7th Annual Energy Conversion Congress and Exposition, and a Tutorial Committee Chair of the IEEE 12th Annual Energy Conversion Congress and Exposition.

Chuan Yao was born in Jiangxi Province, China, in 1986. He received the B.S. degree in the electrical engineering and automatization from Chongqing University, Chongqing, China, in 2007, and the Ph.D. degree in electrical engineering from the College of Electrical and Electronic Engineering, Huazhong University of Science and Technology, Wuhan, China, in 2013.

He is currently with the Wuhan Second Ship Design and Research Institute, Wuhan, China. His main research interests include design and control of power converter, battery management system and renewable energy generation system.